PROCEEDINGS, 44th Workshop on Geothermal Reservoir Engineering
Stanford University, Stanford, California, February 11-13, 2019
SGP-TR-214

High-Resolution Seismic Imaging of a Geothermal Reservoir Using a Cost-Effective Dense Seismic Network

Roland Grittto[1], Donald W. Vasco[2], Lawrence J. Hutchings[3], Kurt T. Nihei[2]

[1]Array Information Technology, 2020 Cedar Street, Berkeley, CA 94709

[2]Lawrence Berkeley National Laboratory, Berkeley, CA 94720

[3]Jarpe Data Solutions Inc., Prescott Valley, AZ 86314

Roland.Gritto@arrayinfotech.com

Keywords: geothermal reservoir, dense seismic array, seismic parameter resolution, seismic reservoir imaging

ABSTRACT

The goal of this study is to utilize a cost-effective high-density seismic array to obtain high-resolution images of reservoir properties at The Geysers geothermal reservoir in northern California. The study is based on the deployment of a dense seismic network over a 5 x 5 km study area in the central Geysers geothermal reservoir. The network configuration resulted from a design study, which employed 100 sensors and analyzed the resulting resolution in elastic parameters such as P- and S-wave velocity estimates. The design study is based on a one-year period of previously acquired microearthquake locations within the study area, 3D P- and S-wave velocity models, and surface topography. Over 3,000 earthquakes were selected, which are densely distributed and cluster in various locations of the region. Based on the hypocenter locations, the 3D velocity models and the various network designs of seismic stations in the study area, synthetic P- and S-wave travel times were computed using an eikonal solver. The algorithms used to estimate model parameter resolution of our seismic velocity estimates were based on (a) a method for computing singular values of large sparse systems values with an iterative Lanczos scheme to obtain quantitative resolution and (b) by 3D inversion for earthquake hypocenters and velocity structure based on absolute and double difference travel times to obtain qualitative resolution estimates. We present the effects of various network topologies including regular and irregular shaped network geometries with a varying number of sensors and incorporate the influences of surface topography on the resolution of the reservoir parameters. The results of the design study were subsequently used to deploy a high-density network of autonomous seismic sensors at The Geysers. The ultimate goal of the study includes the application of rock physics models and theory to the seismic imaging results to derive mechanical properties that are relevant for reservoir engineers.

1. INTRODUCTION

In recent past, the availability of inexpensive seismic sensors has led to the use of passive seismic networks with dense station coverage to investigate shallow and deeper structures of the Earth's crust. The resulting high-density seismic data sets have been used to, i.e., assess seismic hazard in the Los Angeles Basin (Bowden et al., 2015), to perform high-resolution imaging of the fault structure below Long Beach (Lin et al., 2013; Nakita et al., 2015), to investigate the magmatic resource of Mount St. Helens (Wang et al., 2017) and to investigate the structural controls of the Upper Rhein Graben near the Soultz-sous-Forêts and Rittershoffen geothermal reservoirs (Lehujeur, 2018). While the use of passive seismic networks with dense station coverage is only emerging as a tool to gain high-fidelity insight into the structural controls of geothermal reservoirs, commercial utilization of this technique is common place and includes monitoring of hydraulic fractures in oil and gas exploration. (e.g., MicroSeismic; FairfieldNodal; NodalSeismic). The advancement of the commercial technology was largely driven by the economy of scale created by the recent expansion of US shale gas developments. The relative size of the US geothermal and US shale gas industries, as indicated by the number of wells that were drilled in the US during the last week of March 2015, clearly illustrates a lack of an economy of scale for the US geothermal industry: 2 geothermal wells compared to 1,048 oil and gas wells (source: Baker Hughes Inc.). Considering the natural occurrence of micro-seismicity during geothermal operations, passive seismic networks with dense station coverage utilizing inexpensive sensors offer cost-effective strategies to investigate with high-resolution the structural controls of the reservoir. This will enable geothermal operators to more efficiently carry out their operations, including drilling productive wells, avoiding drilling hazards, and optimizing production. However, before dense seismic networks are deployed in the field, the network topology should be investigated to assure best resolution of the reservoir parameters under investigation. In the current paper, we present results of a resolution study for a 100-element seismic network using cost-effective three-component geophones at The Geysers geothermal reservoir.

2. RESOLUTION ANALYSIS OF NETWORK TOPOLOGY

2.1 The Geysers Study Area

In cooperation with Calpine Corp., the operator of The Geysers geothermal field, a study area of 5 km x 5 km was chosen in the central northwest Geysers where additional information on structural control is desired for future reservoir development. The geology and structure of The Geysers is quite complicated, and the velocity structure is highly heterogeneous. To date, there is very little well data constraining the velocity variations at depth. Fortunately, there are a number of tomographic studies that we may use to estimate the smoothly-varying component of seismic velocity in the region of interest. For this work, we adopt recent 3D P- and S-wave velocity

models that were derived for The Geysers geothermal reservoir (Gritto et al., 2013). Earthquake locations were taken from the 2016 LBNL seismic catalog for The Geysers to obtain a representative one-year distribution of seismicity in the study region. A one-year distribution of seismicity is important, because the number of earthquakes depends on the volume of injected water, which is a function of seasonal availability. The selected earthquakes and study area at The Geysers are presented in Figure 1, where the red polygon represents the outline of the steam field, while the green triangles denote the locations of the LBNL permanent seismic network stations. The outline of our 5 km by 5 km study area is given by the black square and the events hypocenters are indicated by the colored dots. A total of 3,389 earthquakes were selected, with a maximum hypocenter depth of 4.5 km, as that was the resolution limit of the 3D P- and S-wave velocity models (Gritto et al., 2013).

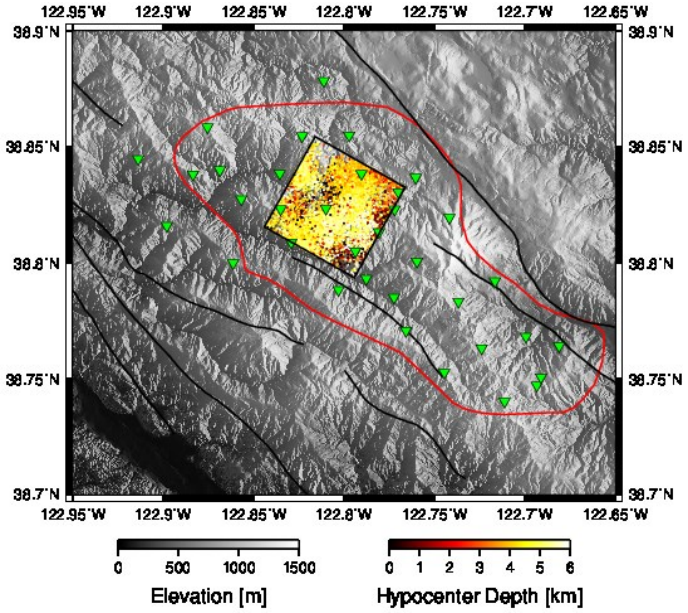

Figure 1: Topographic map displaying the outline of The Geysers steam field (red polygon), the LBNL permanent seismic network stations (green triangles), the 5 km by 5 km study area of the present project (black square) and the distribution of earthquake hypocenters denoted by the colored-dots. Black lines indicate known surface traces of faults.

Based on the hypocenter locations, the 3D velocity models and the various network designs of seismic stations in the study area, synthetic P- and S-wave travel times were computed using an eikonal solver (Podvin and Lecomte, 1991). The algorithm used to estimate the quantitative model parameter resolution of our seismic velocity estimates is based upon the methods for computing singular values of large sparse systems values with an iterative Lanczos scheme developed by Berry (1992). The current implementation is based upon the work by Vasco and Johnson (1998), Vasco et al. (1998) and Vasco et al. (2003). The synthetic travel times were also inverted by 3D inversion for earthquake hypocenters and velocity structure based on absolute and double difference travel times (Zhang and Thurber, 2003) to obtain qualitative resolution estimates. The qualitative resolution estimates are referred to as Derivative Weight Sum (DWS) and represent the total length of ray paths through an inversion node. In the following, the results of our resolution analysis based on various network designs are presented.

2.2 Network Analysis of 100 Regular-Spaced Stations

The first investigated network design comprised a regular-spaced planar array with 100 stations in a 10 by 10 configuration, as shown in Figure 2. The figure also displays the permanent LBNL seismic stations to demonstrate the difference in station density between the two networks. Seismic ray paths and associated travel times were calculated from all 3,389 events to all 100 stations at the surface using an eikonal solver (Podvin and Lecomte, 1991). For a smoothly varying velocity model, such raypaths should be a good representation of the propagating seismic waves (Nolet, 1985). Seismic resolution depends to a large extent on the ray coverage of the small sub-volumes (nodes) of the model. The velocity of a node is constrained by the number and orientation of the seismic waves, and thus the seismic rays that pass through it. Thus, a rough measure of resolution is provided by the density of rays intersecting a given node, or equivalently the total of the ray lengths that pass through a node. In Figure 3, we plot the total sensitivity (the total ray length weighted by the slowness) in horizontal and vertical cross-sections. In the shallow horizontal cross-section in Figure 3a one can see the influence of the stations in the upper portion of the imaging volume, as concentrations of high sensitivity. At intermediate depths (Figure 3b) the variation in ray coverage is influenced by the station distribution, the location of microseismic events, and the variations in ray geometry due to the velocity variations in the model. In the vertical cross-section (Figure 3c), one also observes the role of the seismicity and the low sensitivity at the edges of the model due to a lack of crossing rays in those areas.

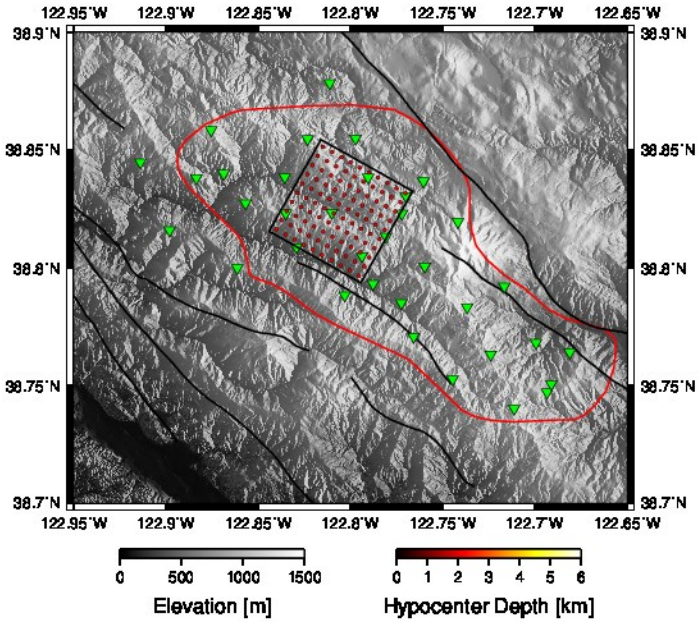

Figure 2: Same as Figure 1, with a 10 by 10 station network design represented by the red dots. Note that the permanent seismic network (green triangles) are not part of this study and plotted only to demonstrate the difference in stations density between the two networks.

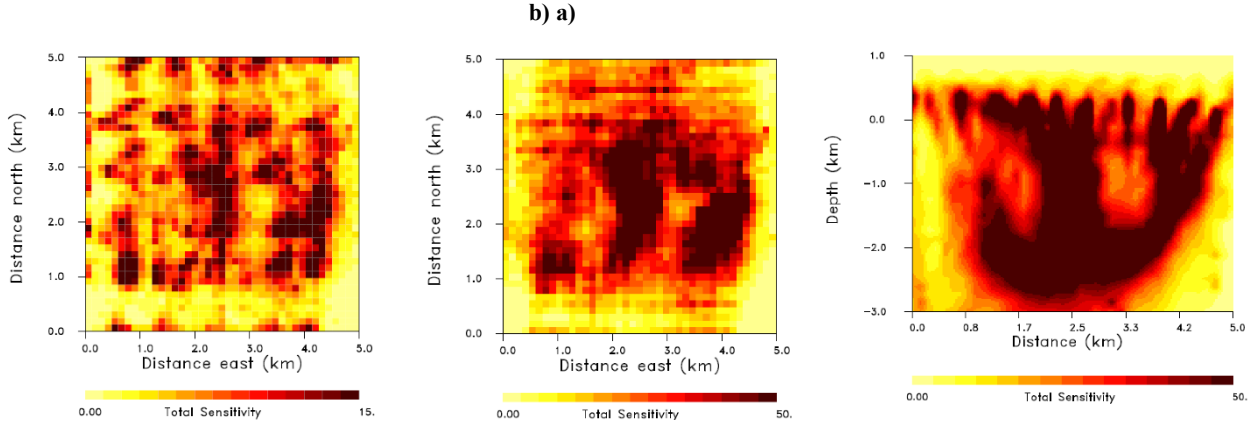

Figure 3: The total ray length in each grid block of the model representing the ray density in each cell. a) Horizontal cross section at a depth of 0.0 km. b) Horizontal cross section at a depth of 1.0 km. c) Vertical cross section in northwest-southeast direction through the center of the model.

The velocity model is parameterized on a 41 (x) by 41 (y) by 51 (z) array of grid blocks, for a total of 85,731 model parameters. The size of the problem precludes the use of an exact calculation of model resolution and necessitates the use of the iterative method. A total of 6,000 Lanczos iterations were used to estimate the model parameter resolution. A singular value cutoff was used to regularize the inverse problem, and singular values less than 1/50th of the peak value were not used.

The resulting diagonal elements of the resolution matrix are plotted in Figures 4. The rows of the resolution matrix are averaging coefficients indicating how each model parameter contributes to the velocity estimates. Due to a normalization in the definition, the values of the diagonal elements provide an indication of how well a parameter is determined, independently of the other model parameters. Thus, a value near 1 indicates that the parameter can be estimated with very little interference from the other model parameters. Diagonal values that are small, close to 0, indicate considerable trade-off with other model parameters. From the 3D plots in Figure 4 it is evident that the resolution decreases with depth. Furthermore, the resolution is greatest below the surface near the stations, where the concentration of raypaths is greatest. The resolution tapers with increasing depth and is concentrated within regions with high seismicity, which is evidenced by two distinct areas with high resolution at the bottom of the study region (Figure 4a). Because

resolution is highest where the concentration of raypaths is highest, high resolution values are typically found in regions of high seismicity and high velocity values, as the latter tend to channel the raypaths through the subsurface. The plot in Figure 4b, which displays resolution estimates in the range 0.2-1.0, demonstrates that the highest resolution values are observed in the shallow subsurface below the seismic stations, due to the highest concentration of raypaths in this region.

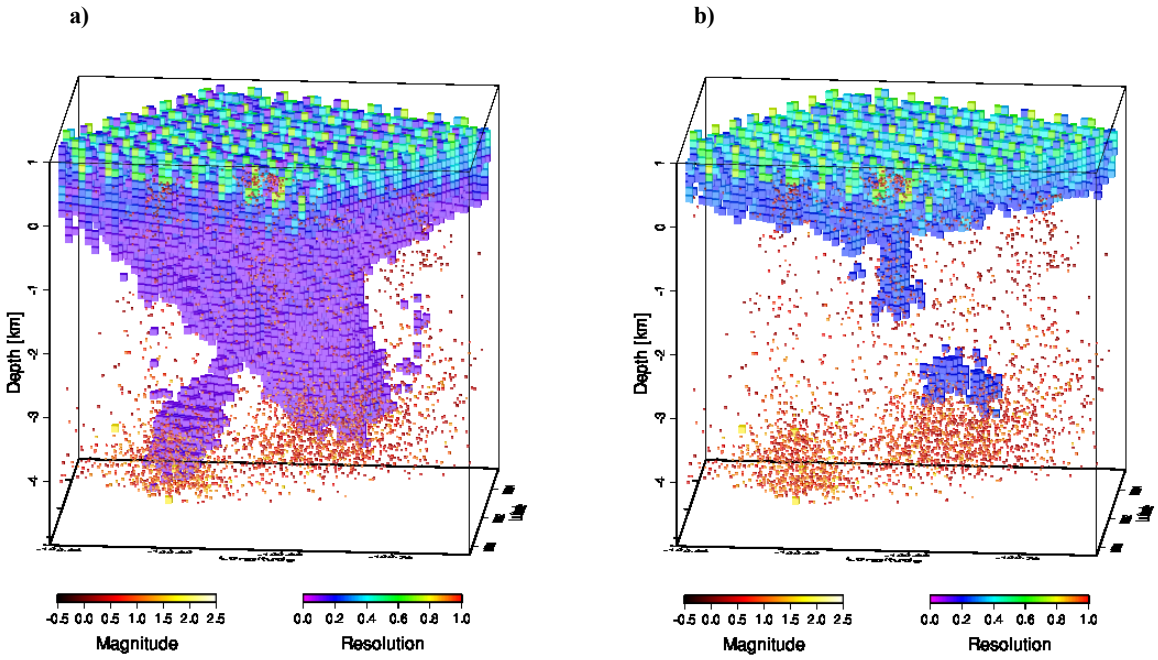

Figure 4: Quantitative resolution estimates of the 3D P-wave velocity in the 5 km by 5 km study area at The Geysers. a) Range of resolution estimates 0.1-1.0. b) Range of resolution estimates 0.2-1.0.

In order to understand the spatial averaging that contributes to a given estimate, we plot some examples of averaging kernels in Figures 5, 6 and 7. For example, in Figure 5 we present side and top views of the averaging kernel associated with a node in the lower part of the study volume (cyan-colored node in Figure 5a). The diagonal element for this grid block has a value below 0.2 (Figure 4a) and it is evident that there is some lateral and specifically vertical averaging with adjacent grid nodes. The increased depth averaging is an indication of poorer depth resolution, due to predominantly vertical raypaths in this section of the model. In Figure 6, we present the averaging kernel for a node in the center of the model. It can be seen that this node exhibits less trade-off with adjacent nodes in vertical as well as in horizontal direction. The reduction in trade-off is due to the better ray density in this region, specifically the improved spatial distribution of rays that cross this part of the model in vertical and horizontal direction. In contrast, Figure 7 displays the case of a node in the near subsurface region of the model below the seismic stations. The results in Figure 4 showed that this is the best resolved region of the model with resolution values of up to 0.6. Despite these high-resolution values, the trade-off of the node in Figure 7 is almost as high as in the bottom of the model, where the actual resolution is lower. The reason, is the ray distribution, which is mainly vertical in this part of the model, leading to trade-off and poor vertical resolution over several layers in the model. The conclusion of this investigation is that parameter estimates of nodes with high resolution values may still trade-off with adjacent nodes in horizontal and/or vertical direction depending on the geometrical quality of ray density. Specifically, when sufficient raypaths cross nodes in horizontal and vertical direction trade-off with adjacent nodes is minimal, while a high number of rays traversing a node in a single direction (either vertically or horizontally) typically results in enhanced trade-off in that same direction.

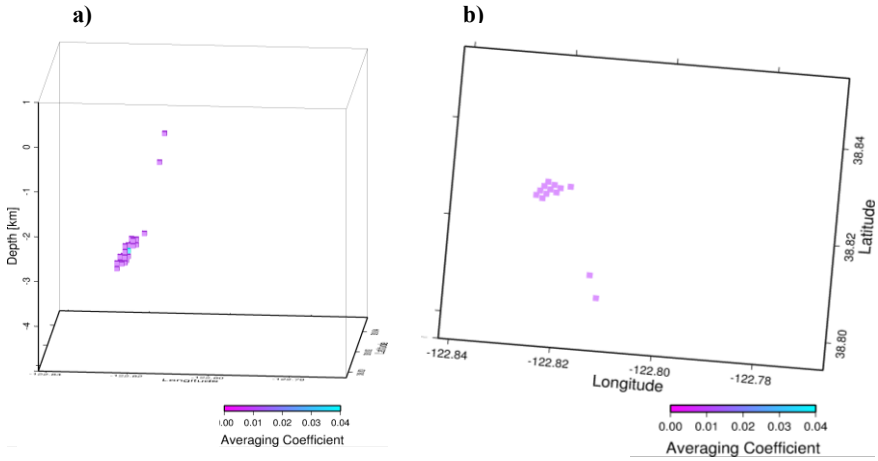

Figure 5: 3D display of an averaging kernel associated with a node at bottom of the model (cyan-colored node). a) Side view. b) Top view.

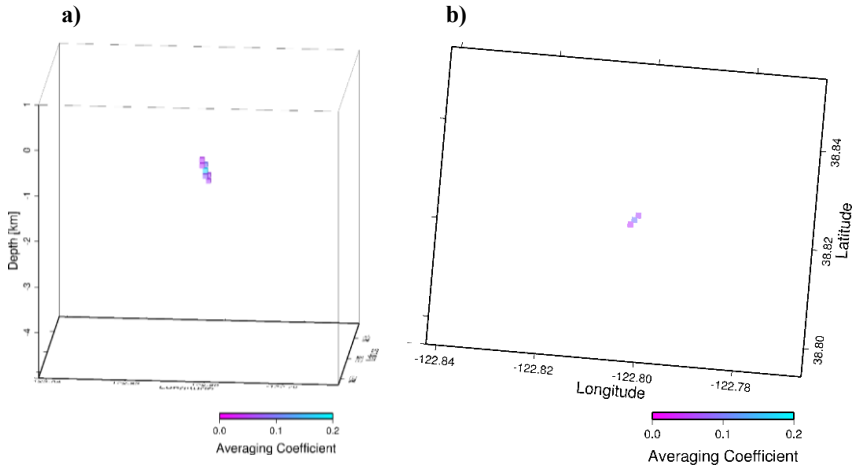

Figure 6: 3D display of an averaging kernel associated with a node in the center of the model (cyan-colored node). a) Side view. b) Top view.

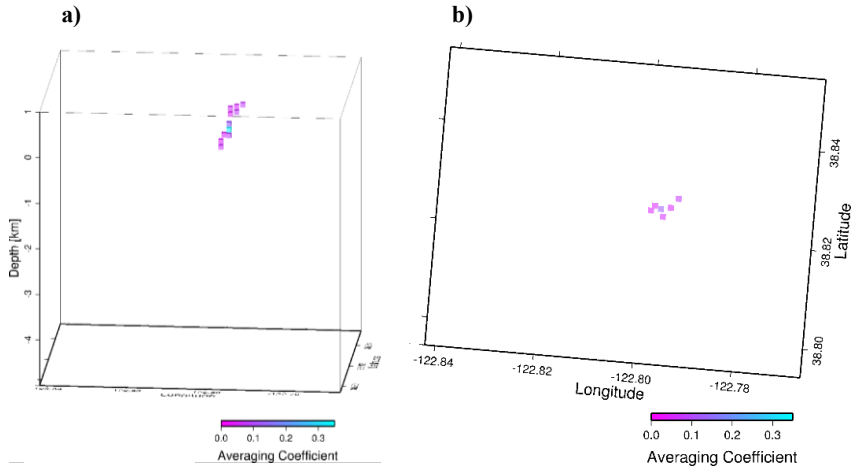

Figure 7: 3D display of an averaging kernel associated with a node in the top of the model (cyan-colored node). a) Side view. b) Top view.

As mentioned above, the resolution of the various seismic network designs was also appraised using a qualitative estimate referred to as Derivative Weight Sum (DWS), which results from inverting the synthetic travel times for 3D P- and S-wave velocity structure and earthquake hypocenter locations (Zhang and Thurber, 2003). The advantage of this approach is computational speed, which allowed us to investigate more network designs than would have been possible with the more formal iterative Lanczos decomposition. Additionally, this method allowed us to investigate the resolution of P- and S-wave velocity estimates simultaneously. At first, we investigate the DWS for the same model presented in Figure 4, to assure comparability between quantitative and qualitative resolution estimates. The derivative weight sum is a measure of total ray length through a node in the model and thus does not vary between 0-1 as the formal model resolution. Therefore, we normalize the DWS by the largest occurring value in the model to provide a resolution range comparable to the quantitative values in the previous cases.

The DWS for P- and S-wave velocity estimates for the 10 by 10 station network is presented in Figure 8. The range from 0.35 to 1.0 was chosen to offer better comparison to the resolution estimate shown in Figure 4. It can be seen, that the overall 3D shape of the resolution for the P-wave estimates in Figures 8a and 4a matches quite well. In the latter figure, the resolution, again, is highest in the near subsurface below the stations, where the ray density is highest and in the lower parts of the model where the earthquakes are clustered. The resolution of the S-wave velocity in Figure 8b, displays lower values compared to those of the P-wave velocity. While in the current examples, the same number of synthetic P- and S-wave arrival times were computed for all possible earthquake-sensor combinations, the weighting factors, representing the quality of the P- and S-wave travel time picks were chosen to be 1 and 0.75, respectively. In typical field situations the quality of S-wave travel time picks is lower than that of the P-wave picks, due to increased noise levels on the seismograms at the onset of S-wave arrivals. The result in Figure 8b denotes the effects of the lower S-wave weighting factor. In real field application, the resolution of the S-wave velocity would still be lower as typical numbers of S-wave phase picks are lower than those of P-wave picks.

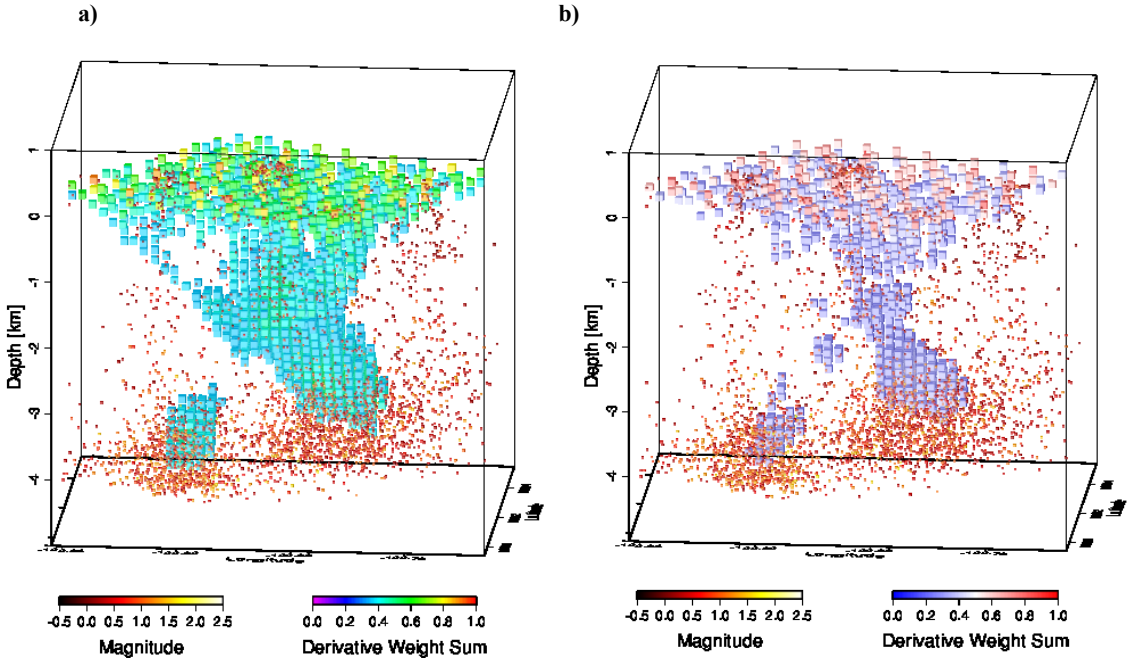

Figure 8: Qualitative resolution estimates of the 3D seismic wave velocity in the 5 km by 5 km study area at The Geysers for a range from 0.35 to 1.0. a) P-wave resolution for a weighting factor of 1.0. b) S-wave resolution for a weighting factor of 0.75.

2.3 Network Analysis of 100 Randomly-Spaced Stations

For this network design, we investigate the effect of a random station distribution on the resolution of the P- and S-wave velocity estimates in the reservoir. The case is similar to that of Section 2.2 in that we assume a planar network topography but allow a random distribution of stations within the study area. The distribution of stations is presented in Figure 9, which reveals areas with clustered stations trading with areas with fewer stations.

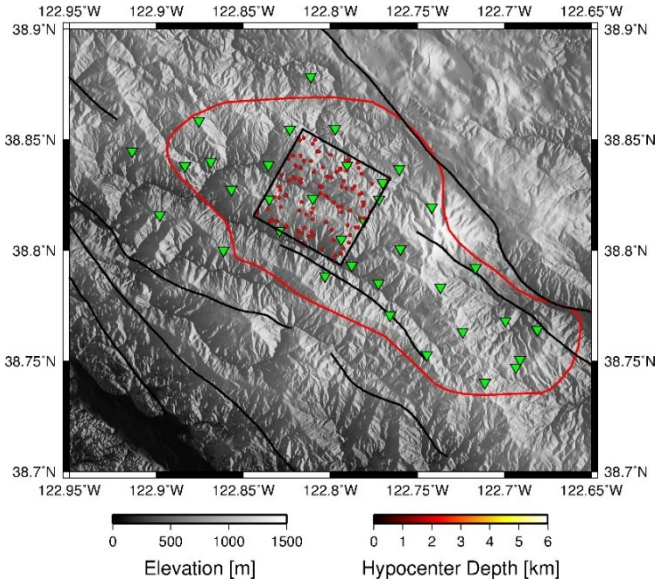

Figure 9: Same as Figure 2, with 100 randomly distributed stations represented by the red dots in the square.

The calculation of raypaths was carried out during the 3D inversion of P- and S-wave travel times for P- and S-wave velocity estimates and the associated computation of the DWS. The resolution plots for the P- and S-wave estimates are presented in Figure 10. During the inversion, equal weighting factors of 1.0 were assigned to both P- and S-wave phase picks. The results are surprising in that the overall structure of the resolution throughout the reservoir is strikingly similar to the results obtained for the regular 10 by 10 stations design presented in Figures 4a, and 8a. The locations of the 100 random stations in Figure 10 are denoted by the red cubes along the surface. Again, the resolution is high in regions where the earthquake density and consequently the density of raypaths is high, which is in the center of the model. Furthermore, the highest resolution overall is observed in the shallow subsurface below the stations where the raypaths converge before reaching the stations. Upon close inspection, it can be seen that the highest resolution is observed in areas where there is a high station density at the surface. Conversely, regions with lower station density exhibit lower near surface resolution.

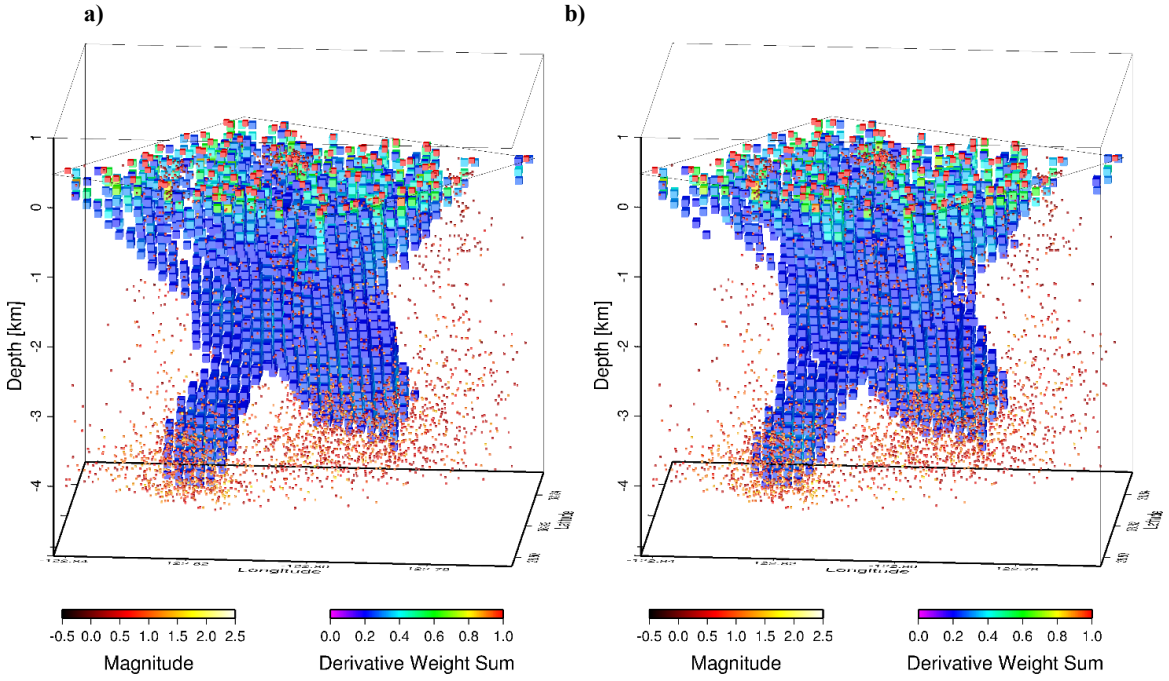

Figure 10: Qualitative resolution estimates of the 3D P-wave velocity in the 5 km by 5 km study area at The Geysers based on a random distribution of 100 stations for a range of resolution from 0.2-1.0. An equal weight of 1.0 was assigned to the P- and S-wave phase picks during the inversion. a) P-wave resolution. b) S-wave resolution. The random stations are denoted by the red cubes at the surface.

In order to better appraise the differences in performance between the regular and randomly spaced network of stations, we calculated the differences in the resolution of the P-wave velocity estimates in Figures 8a and 10a to ascertain their spatial distribution. Figure 11 displays these differences obtained by calculating (resolution values of the regular spaced station network) - (resolution values of the randomly spaced station network). The effects of the different network configurations are plotted in separate figures to provide a clearer picture. The respective stations locations are indicated by the black cubes at the surface. Figure 11a displays the regions where the resolution of the randomly spaced network is higher. It can be seen that these differences are located in the shallow subsurface below the various cluster of stations. This is expected as the cluster of stations aggregate the raypaths below them. Conversely, in regions where the randomly distributed station density is low, the resolution associated with the regularly spaced station configuration is higher (Figure 11b). The surprising lesson from this comparison is that the resolution in the center of the model is very similar in both cases. The conclusion is that given the same number of stations, the resolution in the reservoir is somewhat independent of the station design as long as the region of interest is deep enough below the surface.

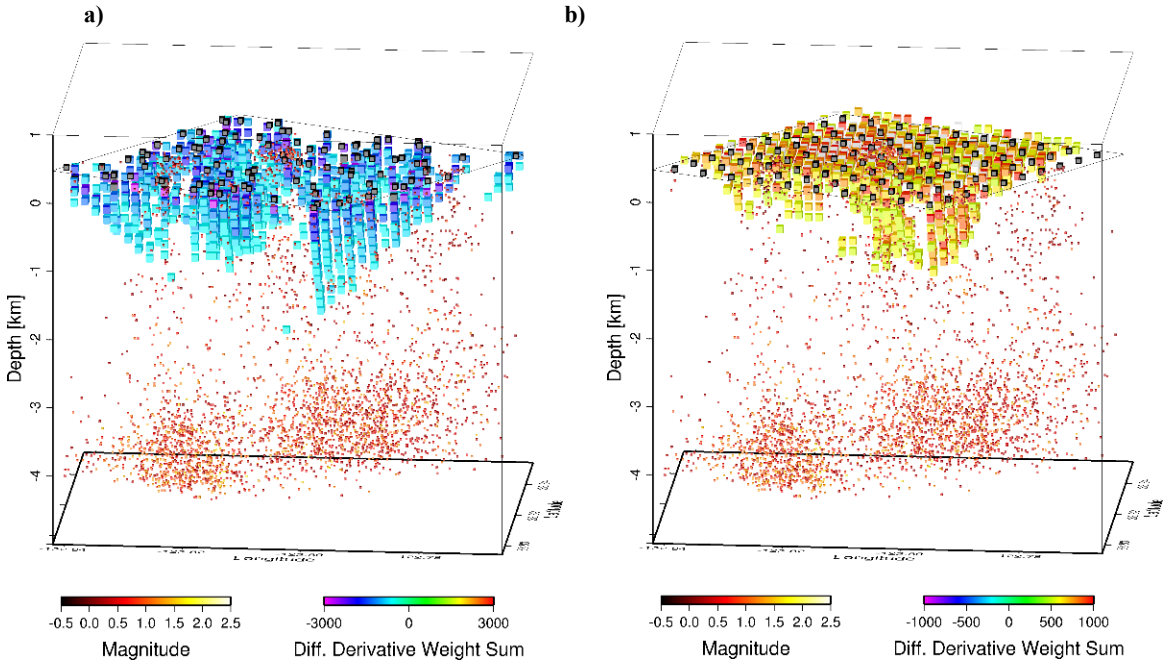

Figure 11: Difference in the resolution of P-wave estimates between the regular spaced network of stations in Figure 8a and the randomly distributed network of stations in Figure 10a. The station locations are indicated by the black cubes at the surface. a) Regions where the resolution estimates for the randomly distributed network are higher. b) Regions where the resolution estimates for the regularly distributed network are higher.

3. CONLUSIONS

We analyzed the resolution of P- and S-wave velocity estimates derived for different seismic network topologies within a 5 x 5 km study area in the central northwest Geysers. The study was based on natural occurring seismicity observed during a one-year period in the study area. The quantitative resolution analysis based on an iterative Lanczos scheme revealed that in general, the resolution of the velocity estimates is greatest below the surface near the seismic stations, where the concentration of raypaths is greatest, while it decreases with depth where intermediate values are concentrated within regions with high velocity estimates and high seismicity. The analysis of resolution trade-off revealed that parameter estimates of nodes with high resolution values may still trade-off with adjacent nodes in horizontal and/or vertical direction depending on the geometrical quality of ray density. Specifically, when sufficient raypaths cross nodes in horizontal and vertical direction trade-off with adjacent nodes is minimal, while a high number of rays traversing a node in a single direction (either vertically or horizontally) typically results in enhanced trade-off in that same direction. Low number of S-wave phase picks as well as poor quality picks, have an adverse effect on the resolution of S-wave velocity estimates. When a dense seismic network is available, the resolution in the reservoir is somewhat independent of the station design as long as the region of interest is deep enough below the surface. These are welcome findings for seismic imaging in mountainous and wooded terrain, which may not permit exact station placement as determined by numerical modeling studies. However, when the number of seismic stations in a network becomes too low, comparable resolution for the regular-spaced versus randomly-spaced network design is no longer given. In this case, a regular-spaced network design yields the higher resolution for the P- and S-wave estimates in the reservoir. In our presentation we will cover additional network topologies not covered in this paper.

REFERENCES

Berry, M., (1992), Large scale singular value computations, *Internat. J. Supercomp. Appl*., **6**, 13-49.

Bowden, D.C., V.C. Tsai, and F.-C. Lin, (2015), Site amplification, attenuation, and scattering from noise correlation amplitudes across a dense array in Long Beach, CA, *Geophys. Res. Lett*., **42**, 1360–1367, doi:10.1002/2014GL062662.

FairfieldNodal, http://www.fairfieldnodal.com/.

Gritto, R., S.H. Yoo and S.P. Jarpe, (2013), 3D seismic tomography at The Geysers geothermal field, CA, USA, *Proceedings of Thirty-Eighth Workshop on Geothermal Reservoir Engineering*, Stanford University, California, 11-13 February, 2013.

Lehujeur, M, J. Vergne, J. Schmittbuhl, D. Zigone and A. Le Chenadec, (2018), Reservoir Imaging Using Ambient Noise Correlation From a Dense Seismic Network, *J. Geophys. Res*., **123**, 8, 6671-6686.

Lin, F.-C., D. Li, R.W. Clayton, and D. Hollis, (2013), High-resolution 3D shallow crustal structure in Long Beach, California: Application of ambient noise tomography on a dense seismic array, *Geophys*., **78**(4), Q45–Q56, doi: 10.1190/GEO2012-0453.1.

MicroSeismic, http://www.microseismic.com/.

Nakata, N., J. Chang, J.F. Lawrence, and P. Boué, (2015), Body wave extraction and tomography at Long Beach, California, using ambient noise interferometery, *J. Geophys. Res*., **120**, 1159-1173, doi: 10.1002/2015JB011870.

NodalSeismic, www.nodalseismic.com/.

Nolet, G., (1985), Solving or resolving inadequate and noisy tomographic systems, *J. Comput. Phys*., **61**, 463-482.

Podvin, P., and I. Lecomte, (1991), Finite difference computation of travel times in very contrasted velocity models: A massively parallel approach and its associated tools, *Geophys. J. Int*., **105**, 271–284.

Vasco, D. W., L.R. Johnson and O. Marques, (1998), Resolution, uncertainty, and whole Earth tomography, *J. Geophys. Res*., **18**, 2022, doi:10.1029/2001JB000412.

Vasco, D. W. and L.R. Johnson, (1998), Whole Earth structure estimated from seismic arrival times, *J. Geophys. Res*., **103**, 2633-2671.

Vasco, D. W., J.E. Peterson and E.L. Majer, (1998), Resolving seismic anisotropy: Sparse matrix methods for geophysical inverse problems, *Geophysics*, **63**, 970-983.

Wang, Y, F.-C., Lin, B., Schmandt, J., Farrell, (2017), Ambient noise tomography across Mount St. Helens using a dense seismic array, *J. Geophys. Res*., **122**, 1159-1173, https://doi.org/10.1002/2016JB013769.

Zhang, H. and C.H. Thurber, (2003), Double-Difference Tomography: The Method and Its Application to the Hayward Fault, California, *Bul. Seism. Soc. Am*., **93**, 1875–1889.